ADVANCED FUNCTIONAL MATERIALS
www.afm-journal.de

Topological Exciton Polaritons in Compact Perovskite Junction Metasurfaces

Soo-Chan An, Yeonsoo Lim, Ki Young Lee, Daegwang Choi, Seongheon Kim, Su-Hyun Gong, Jae Woong Yoon, and Young Chul Jun**

Exciton polaritons are hybrid light-matter quasi-particles that hold exceptional opportunities for future optoelectronic devices. Taking the synergic advantages of room-temperature perovskite excitons and topological photonic structures, topological exciton-polaritons are experimentally demonstrated in organic–inorganic hybrid perovskite thin films. Topological junction structures based on perovskite gratings are realized using a momentum-space analog of the 1D Dirac system. Desired enhancement phenomena are observed including narrow-beam polariton emission from a tightly localized junction region, polaritonic nonlinearity boost, and enhanced luminescence. These remarkable features are obtained from highly compact devices with footprint widths on the order of a few micrometers and are efficiently tailorable with simple unit-cell geometry control. Therefore, the proposed approach can be a powerful platform for room-temperature topological exciton-polaritons and concomitant device applications.

1. Introduction

Exciton polaritons are hybrid light-matter quasi-particles formed by strong coupling between photonic modes and excitons.[1] They inherit their characteristics from both photonic and excitonic components, and thereby the advantages of light and matter can be efficiently combined in a single entity. These features include low effective mass, ballistic transport, strong nonlinearity, and enhanced sensitivity to external electric and magnetic fields, which provide promising opportunities for future device applications[2] such as all-optical ultrafast switches and logic gates,[3] polaritonic lasers,[4] quantum simulators,[5,6] and quantum polariton devices.[7–9]

Cryogenic conditions are essential in general for exciton-polariton studies employing conventional semiconductor systems such as GaAs quantum wells and quantum dots. Recent studies have proposed room-temperature exciton polariton materials.[10] Among many others, halide perovskite materials have attracted special attention.[11] They have been extensively studied for use in solar cells and light-emitting diodes.[12,13] Recently, both organic–inorganic hybrid and all-inorganic perovskite materials have attracted significant interest for exciton-polaritons owing to their exceptional properties, such as large oscillator strength and binding energy, large exciton nonlinearity, and broad compositional and structural tunability.[14–16]

Various nanophotonic structures have been employed to form and control exciton polaritons based on perovskite materials. These include planar cavities,[17–21] photonic crystals,[22–26] coupled photonic cavity arrays,[27] and resonant particles or wires.[28] Considering potential applications that take full advantage of room-temperature operation and tailorable nanophotonic properties, topological photonic structures are of increasing interest for exciton-polaritons.[29–31] This is because they potentially provide inherent robustness against structural imperfections and environmental disturbances, as well as additional degrees of control freedom over photonic localization and emission properties.[32,33] Previously, a direct *real-space* analogy to the Su–Schrieffer–Heeger (SSH) model was introduced using 1D dimer lattices.[34–36] A 1D zigzag configuration of identical dielectric resonators was also considered.[37] Similar zigzag chains of coupled resonators have been employed for topological edge states in exciton-polariton systems,[38,39] successfully demonstrating the experimental feasibility of the polariton SSH state in real space.

Here, we combine topological guided-mode resonances (GMRs) with perovskite excitons to realize robust topological exciton-polaritons at room temperature. We employ a

S.-C. An, Y. Lim, S. Kim, Y. C. Jun
Department of Materials Science and Engineering
Ulsan National Institute of Science and Technology (UNIST)
Ulsan 44919, Republic of Korea
E-mail: ycjun@unist.ac.kr
K. Y. Lee, J. W. Yoon
Department of Physics
Hanyang University
Seoul 04763, Republic of Korea
E-mail: yoonjw@hanyang.ac.kr
D. Choi, S.-H. Gong
Department of Physics
Korea University
Seoul 02841, Republic of Korea
Y. C. Jun
Graduate School of Semiconductor Materials and Devices Engineering
UNIST
Ulsan 44919, Republic of Korea

The ORCID identification number(s) for the author(s) of this article can be found under https://doi.org/10.1002/adfm.202313840

DOI: 10.1002/adfm.202313840

momentum-space analog of the 1D Dirac system to diffractive exciton polariton states. In stark contrast to conventional topological photonic structures in the direct spatial analogy of solid-state systems, our proposed approach creates Jackiw–Rebbi (JR) states in a topological grating junction. Importantly, these diffractive JR states inherently allow direct access to the out-of-plane radiation continuum and enable localized light-matter enhancement phenomena without an additional experimental probe or structural perturbation.

The optical analogy of the JR states has been studied in several topological photonic structures, such as coupled resonators or waveguides.[40–42] In these structures, each unit cell supports multiple localized states whose intra-cell and inter-cell interactions produce Hermitian topological effects basically pertaining to those in solid-state atomic lattices. In our momentum-space analog, however, spatially delocalized guided modes form spectrally localized states in the wave-vector domain, and they are essentially non-Hermitian because of their inherent coupling with the radiation continuum in the surrounding media. A photonic JR state is formed in a junction of the two different grating systems, which hold the photonic band inversion and topological phase transition between them. One grating system has a topological phase while the other with inverted band polarity holds a trivial phase. In the junction made of these two gratings, a topological localized state appears at the junction interface.[43,44] The momentum-space analog provides extra degrees of control freedom that can be used to efficiently realize novel topological cavities.[45–48]

We experimentally realize a topological junction of perovskite gratings that combine a compact lateral size in real space with narrow discrete responses in momentum space. The mid-gap polariton JR state formed at the gamma point ($k_x = 0$) can be useful for polariton devices because polaritons can be locally confined and accumulated at an energy minimum state. The spatial and angular distributions of the polariton JR state can be tailored by appropriately designing the Dirac mass or, equivalently, groove-width distributions. Detailed reflectance and photoluminescence (PL) measurements are conducted in both momentum and real spaces to clearly demonstrate the remarkable features of topological exciton-polaritons. Polariton confinement and the desired enhancement phenomena are demonstrated in highly compact and simplified grating structures, including highly enhanced, narrow-beam (<5°) emission and polaritonic nonlinearity boost. The idea of topological grating junctions can be readily extended to other excitonic material systems. Therefore, our results suggest a powerful experimental platform for further extensive development of room-temperature topological exciton-polaritons and concomitant device applications.

2. Results and Discussion

2.1. Formation of Topological Exciton Polaritons in a Compact Junction

Figure 1a shows the schematic of a perovskite junction comprising two topologically distinct grating regions. Linear grating patterns were first defined on a quartz substrate using electron-beam lithography and reactive-ion etching. A 2D layered organic–inorganic hybrid perovskite [$(C_6H_5C_2H_4NH_3)_2PbI_4$] layer was spin-coated onto the patterned quartz substrate, followed by annealing and overcoating with a thick poly(methyl methacrylate) (PMMA) layer. The details of the fabrication conditions are provided in the Experimental Section. Figure 1b shows the optical microscope images of the two fabricated samples for the topological junctions of 10 and 3-μm-wide grating regions, respectively. The different colors between the left and right gratings are due to the different amounts of perovskite materials. Note that the dielectric metasurface in our sample is defined by the perovskite material itself as shown in the schematic. In Figures S1 and S2 (Supporting Information), we present plane and cross-sectional scanning electron micrographs of the fabricated samples, confirming the reliability of our established fabrication procedure.

The 2D perovskite layer used here produces strong excitonic responses because of its self-assembled quantum-well layer structure, resulting in the tight confinement of electron-hole pairs and subsequent large binding energy and oscillator strength.[14,15] These characteristics further lead to the efficient generation of room-temperature exciton polaritons in our structures. The X-ray diffraction, absorption, and photoluminescence spectra, and optical-constant characterization data for the perovskite material are provided in Figure S3 (Supporting Information).

In the proposed structure, the perovskite layer has a higher refractive index than the surrounding medium (PMMA and quartz) and supports the fundamental guided photonic mode within the spectral region of interest from 500 to 600 nm. The measured refractive indices of the perovskite film are shown in Figure S3d (Supporting Information). The refractive indices of PMMA and quartz are 1.49 and 1.5, respectively, in the visible range. The fundamental guided photonic mode having the greatest local density of states in the perovskite layer couples strongly with the perovskite excitons. The counter-propagating guided modes are coupled to each other through the second-order Bragg reflection by the grating structure.[49,50] This diffractive coupling results in Bloch–Floquet eigenstates with their characteristic band topology determined by the Bragg reflection phase angle, which is conveniently switchable between zero and π for the trivial and topological phases, respectively, by means of grating groove-width control. Consequently, a perovskite junction with two topologically distinct waveguide gratings can create a topological JR state localized at the junction interface.

To design an optimal junction structure for experimental realization, it is crucial to derive design-parametric conditions for the desired topological phase transition within a spectral range of acceptably strong exciton responses around the exciton energy level. Therefore, we first derive the conditions for the purely photonic topological phase transition. For topological GMRs, the bandgap center $\lambda_c \approx n_{eff}\, p$ and bandgap width $\Delta\lambda \approx 2(v_g\lambda_c)^2(hc)^{-1}|m|$ with a Dirac mass m are given by[43,44]

$$m \approx \frac{hc}{\lambda_c {v_g}^2}\left(\rho_1 {\varepsilon_1}^2 - \rho_2\varepsilon_2\right) \quad (1)$$

here, n_{eff} is the effective index of the guided mode, p is the period of the grating, v_g is the group speed of the guided mode, h is the Planck constant, c is the speed of light in vacuum, ρ_i is the normalized rate of coupling between the two counter-propagating guided modes through the i-th order diffraction

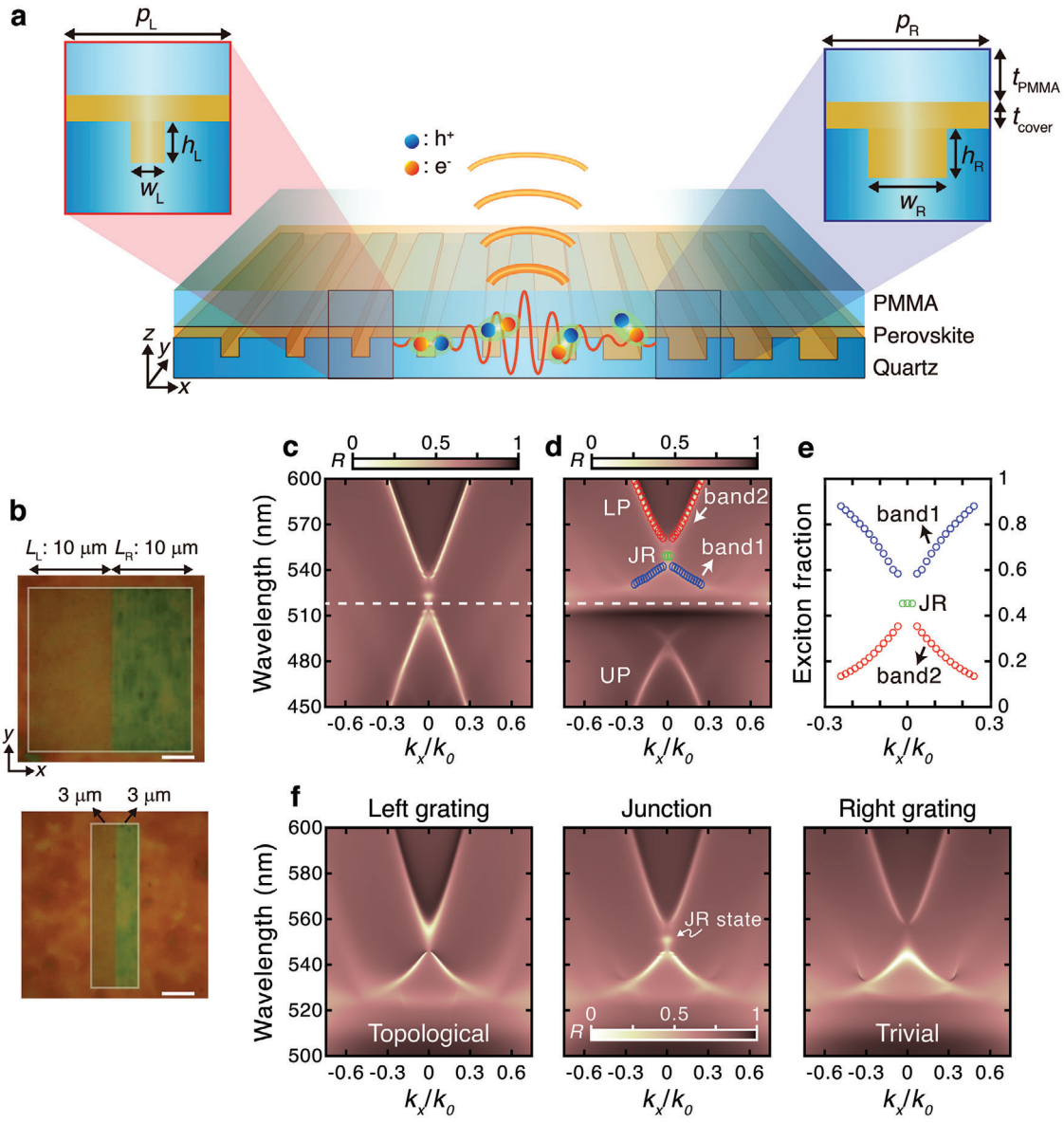

Figure 1. Formation of topological exciton polaritons in a compact junction. a) Schematic of the perovskite junction metasurface. b) Optical microscopy images (real color) of the junction metasurface with different lateral grating sizes. The length in the y direction is fixed as 20 μm. The boundaries of the grating patterns are indicated as gray lines. Scale bar: 4 μm. Simulated reflectance spectrum for c) passive and d) active structures. UP: upper polariton, LP: lower polariton. Incident light is polarized parallel to the grating line. The passive structure assumes a constant index of $n = 2.15$ for 2D perovskite material. For the active structure, the optical constants with a single Lorentzian function are used in simulations (Experimental Section). $k_0 = 2\pi/\lambda$ (where λ is a free space wavelength) and $k_x/k_0 = \sin\theta$ (where θ is an incidence/emission angle measured in the air). e) Exciton fractions for the LP branch. f) Simulated reflectance spectra of the left grating, junction, and right grating ($p_L = 310$ nm, $p_R = 290$ nm, $w_L = 80$ nm, $w_R = 190$ nm, $h_L = 85$ nm, $h_R = 100$ nm, $t_{PMMA} = 200$ nm, and $t_{cover} = 60$ nm). The experimentally measured optical constants are used. The effective mode index n_{eff} is related to the bandgap center wavelength (λ_c) and grating period (p): $n_{eff} \approx \lambda_c/p$. The effective mode indices of the left and right gratings are estimated to be $n_{eff} \approx 1.77$ and 1.90, respectively. The group velocity can be obtained from the slope of the dispersion band near the photonic bandgap ($v_g \approx 0.22c$).

channel, and ε_j is the spatial Fourier coefficient of the dielectric function in the grating layer at the j-th harmonic order. The bandgap center λ_c can be easily matched to a certain desired point, such as the exciton energy level, by tuning the period p for a given n_{eff}.

In contrast, the bandgap width $\Delta\lambda$ and topological phase determinations require precise tuning of the Dirac mass m in its absolute magnitude and sign, respectively. Note that the waveguide grating is in the topological phase for $m < 0$ or in the trivial phase for $m > 0$. Applying the expression for ε_j in terms of the structural parameters associated with Equation (1), we obtain an alternative expression for the Dirac mass as

$$m \approx \frac{hc}{\lambda_c {v_g}^2} F\Delta\varepsilon \left[\rho_1 F\Delta\varepsilon \, \mathrm{sinc}^2(F) - \rho_2 \mathrm{sinc}(2F)\right] \quad (2)$$

where $\Delta\varepsilon$ is the dielectric constant difference between the high-index and low-index parts in the grating layer, F indicates the ratio of the groove width w to the period p, that is, $F = w/p$, and the normalized sinc function is defined as $\mathrm{sinc}(a) = \sin(\pi a)/(\pi a)$. In this expression, F is immediately identified as the key factor that determines the topological phase. In particular, the characteristic numerical property of the sinc function implies that $m > 0$ (trivial phase) for $F > F_c$ or $m < 0$ (topological phase) for $F < F_c$, where F_c is the critical groove width-to-period ratio for $m = 0$. In addition, m vanishes at the two boundary points $F = 0$ and 1, regardless of the specific configurations of the other factors. Therefore, the largest bandgap width is obtained around the two median points at $F = F_c/2$ for the topological phase domain $0 < F < F_c$ or $F = (1+F_c)/2$ for the trivial phase domain $F_c < F < 1$. We note here that this Dirac mass tunability is unique to the momentum-space analog of the 1D Dirac system. The topological phase in the conventional real-space analog is determined by the spatial asymmetry of inter-atomic coupling, whereas in our approach, it is determined by the spectral asymmetry of the inter-harmonic coupling through different diffraction channels. Therefore, the topological phase transition is readily obtained without requiring apparent spatial asymmetry or complicated coupled-resonator array configurations, and thus the momentum-space approach can be more favorable for compact and reliable device development.

We design the perovskite GMR structures (uniform gratings) on this basis. In Figure S4 (Supporting Information), we present the numerical calculation results of the reflection spectra for passive, non-excitonic waveguide gratings with a constant refractive index of $n = 2.15$ for the perovskite material. Therein, the purely photonic topological phase transition at the critical groove width $w = w_c = 140$ nm is evident as the super-radiant broad resonance and vanishingly narrow sub-radiant resonance features at the two band edges flip their locations across the $w = w_c$ condition. The sub-radiant resonance at the band edge is often referred to as a symmetry-protected bound state in the continuum.

From this result, we numerically create a junction of two topologically distinct GMR gratings with their groove widths and periods finely tuned so that their bandgaps match with each other. The simulated reflectance spectrum is shown in Figure 1c, and we identify the purely photonic JR state resonance right above the exciton level (dashed horizontal line at 518 nm). Although we optimize the junction metasurface structure such that the bandgaps of the left and right grating regions exactly match to create a localized JR state with the strongest lateral confinement, the bandgap matching is not a necessary condition. In general, the JR state energy is determined by

$$E_{\mathrm{JR}} = \frac{m_{\mathrm{L}} E_{\mathrm{cR}} + m_{\mathrm{R}} E_{\mathrm{cL}}}{m_{\mathrm{L}} + m_{\mathrm{R}}} \tag{3}$$

where m_{L} and m_{R} are the Dirac masses of the left and right regions of a junction, respectively, and E_{cL} and E_{cR} are the mid-gap energies of the left and right regions.[43] This formula implies that a JR state always exists as long as the energy ranges of the two topologically distinct bandgaps overlap.

The exciton-polariton JR state is now directly obtained by applying the excitonic response to the perovskite layer, as shown in Figure 1d. The excitonic Lorentz oscillator model was used to determine the optical constant of the perovskite material in the simulation, as described in detail in the Experimental Section. The strong coupling between the photonic guided mode and perovskite exciton results in the upper and lower polariton branches (UP and LP, respectively, in Figure 1d). Such a light-matter hybrid system is described using the following two-level model:

$$\begin{pmatrix} E_{ex} + i\gamma_{ex} & g \\ g & E_{ph} + i\gamma_{ph} \end{pmatrix} \begin{pmatrix} \alpha \\ \beta \end{pmatrix} = E_{\pm} \begin{pmatrix} \alpha \\ \beta \end{pmatrix} \tag{4}$$

here, E_{ex} and E_{ph} are the energy levels of the exciton and pure photonic modes, respectively, γ_{ex} and γ_{ph} are the corresponding linewidths, and g is the coupling energy between them. $E_{\pm}$ are the two eigenvalues corresponding to the UP and LP branches, respectively. The eigenvector components α and β are the Hopfield coefficients that represent the exciton and photon fractions in the exciton-polariton by $|\alpha|^2$ and $|\beta|^2$.

This model yields the exciton-polariton energy

$$E_{\pm} = \frac{1}{2}\left[E_{\mathrm{ex}} + E_{\mathrm{ph}} + i(\gamma_{\mathrm{ex}} + \gamma_{\mathrm{ph}})\right] \pm \sqrt{g^2 + \frac{1}{4}\left[E_{\mathrm{ex}} - E_{\mathrm{ph}} + i(\gamma_{\mathrm{ex}} - \gamma_{\mathrm{ph}})\right]^2} \tag{5}$$

and the Rabi splitting

$$\hbar\Omega = \sqrt{4g^2 - (\gamma_{\mathrm{ex}} - \gamma_{\mathrm{ph}})^2} \tag{6}$$

The Rabi splitting and exciton fractions are conveniently obtained by fitting $E_{\pm}$ to the simulated polariton bands in the reflection spectrum. The extracted parameters at $k_x = 0$ is given in **Table 1**. We obtain a Rabi splitting of ≈260 meV. The polariton JR state in the LP branch appears at ≈550 nm in the middle of the bandgap. The exciton fractions of the LP branch are shown in Figure 1e. The JR state retains an exciton fraction of ≈0.45, which further confirms the formation of the exciton photon hybrid matter at our junction metasurface.

Table 1. Extracted parameters for Equation (5) at $k_x = 0$.

Parameter	E_{ex}	E_{ph}	E_+	E_-	γ_{ex}	γ_{ph}	g
Value [eV]	2.394	2.370	2.52	2.25	0.03	0.011	0.131

As a final step of the design, we apply this junction metasurface structure to a realistic numerical simulation with the experimental optical constants of the perovskite layer provided in Figure S3d (Supporting Information). Figure 1f shows the simulation results of the LP branch reflection spectra for the left grating, junction, and right grating. The band inversion between the left and right gratings clearly indicates a topological transition. In the left grating, the leaky mode appears in the longer wavelength region of the bandgap while the nonradiative mode (or bound state in the continuum) exists in the short wavelength region. This corresponds to a topological phase. The right grating exhibits the opposite behavior and holds a trivial phase. In the topological junction made of these two gratings, a topological interface state appears in the middle of the photonic bandgap.[43] We confirm all the essential features desired in the topological exciton polariton. The polariton JR state appears at $k_x = 0$ as a discrete spot-like state.

2.2. Momentum-Space Measurements of Reflectance and Photoluminescence Spectra

To experimentally investigate the polariton modes (localized JR state and delocalized GMRs), we measured angle-resolved reflectance and PL spectra in momentum space using a custom-built Fourier-plane setup (see Experimental Section). We fabricated uniform gratings with different w values in the range of 55 nm $\leq w \leq$ 210 nm for a fixed period p = 305 nm and measured their reflectance spectra, as shown in Figure S5 (Supporting Information). The measurement results yield a critical groove width w_c of ≈145 nm, which indicates the topological phase for $w < w_c$ or the trivial phase for $w > w_c$. Subsequently, we obtain the critical groove width-to-period ratio, $F_c = w_c/p = 0.475$.

The polariton JR state formation was systematically studied by fabricating a large set of junction metasurfaces with left and right gratings in the topological and trivial phases, respectively. In particular, for fixed groove widths, the grating period was gradually varied from 285 to 310 nm. Figures S6–S8 (Supporting Information) show the measured reflectance spectra, where clear JR state peaks were observed in many samples with acceptably good bandgap overlap. Figures S9–S11 (Supporting Information) represent the corresponding PL spectra, which manifest the strong JR state emission in the vertical direction. The PL spectra were measured using a continuous-wave diode laser at 450 nm as the excitation source. **Figure 2** shows a representative case of these data. Figure 2a,b compares the reflectance and PL spectra, respectively, of the left grating, junction, and right grating. They reveal all the essential topological features, including the polariton JR state resonance, which is in excellent agreement with our theoretical prediction in Figure 1. Figure S12 (Supporting Information) shows more comparisons, which confirm the formation of the topological JR state at the center of the bandgap.

Intriguingly, the JR state emission is highly directional in the vertical direction (k_x = 0) (Figure 2c). Additional data in Figure S13 (Supporting Information) confirm the same feature. In all cases, PL occurred within a narrow angular domain of < 5°. Therefore, the observed PL spectra experimentally demonstrate the topological beaming effect and further suggest that our approach could enable efficient beam shaping of the exciton-polariton emission via Dirac mass engineering around the topological junction.[44] Note also that the JR state emission is slightly shifted in the negative k_x direction. The dielectric junction metasurface in our sample is formed by the perovskite material itself (Figure 1a). Because the left and right gratings have different fill factors, they have different amounts of the perovskite material. Therefore, we think that, in our measurements, more emitters can be possibly excited in the right grating (having a larger fill factor). This can, in turn, induce slight asymmetry (0.5°–1°) in the angular profile of the emission. We find that the junction structure exhibits a slightly higher PL intensity for the negative group velocity branch than the other (Figure 2b).

We also estimated the PL enhancement factor (Figure 2d,e), which was obtained by normalizing the PL spectrum to the bare exciton PL spectrum in the unpatterned flat region of the sample. See also Figure S12 (Supporting Information) for additional data. The perovskite emission intensity is normally expected to decay fast at the shoulder of the bare exciton peak (dashed line in Figure 2d). However, the measured emission spectra from the perovskite junctions manifest an extremely strong PL enhancement in the polariton JR state. The JR state exhibits a significantly larger PL enhancement than the neighboring GMR bands. The strong JR state emission is potentially important for polaritonic light sources and devices.

2.3. Topological Light Localization and Polariton Confinement

The strong emission enhancement at the polariton JR state resonance is closely related to the tight lateral confinement. Therefore, we further investigated the lateral localization property of the observed effect. In **Figure 3**a, we show the angle-resolved PL spectra from the junction metasurfaces as tightly focused excitation laser beam scans across the junction in the sequence illustrated in Figure 3b. The grating parameters are the same as those in Figure 2. We observe a strong JR state emission only for a localized excitation region near the junction, in contrast to the normal GMR features that are delocalized over the entire grating region. Figure 3c shows the normalized PL intensity at the JR state resonance center as a function of the position of the excitation beam from the junction. When the focused laser spot moves away from the junction interface, the JR state emission intensity rapidly decreases. The measured profile is consistent with the calculated mode profile in Figure 3c. This again confirms the formation of the topological interface state in our junction metasurface. The field profile in Figure 3c shows exponential profiles on both sides of the junction, which are consistent with zero cavity length in our topological cavity.

The observed lateral confinement of the JR state compared with the delocalized GMRs implies a small footprint size of the grating system as a device. We further verified polariton confinement by directly reducing the lateral size of the grating. In Figure 3d,e, we show the sample image and PL spectra of 6-μm-wide devices with three different configurations: two uniform gratings in the topological (left side) and trivial (right side) phases, respectively, and a junction of two half-pieces of them (therefore, 3 μm on each side). The conventional GMR bands are significantly blurred and suppressed compared to those obtained from the 20-μm-wide device because of the degradation of the resonance quality factor with footprint size reduction in the GMR gratings. In contrast, the emission spot of the localized JR state maintains its tightness in both the wavelength and wave-vector domains. Therefore, we experimentally confirmed that our proposed approach can be used to readily obtain highly compact and controllable exciton-polariton systems on the scale of a few micrometers.

2.4. Real-Space PL Imaging with Momentum-Space Filtering

We also conducted real-space measurements of the polariton JR state emission to verify that the spot-like emission near k_x = 0 originates from the interface state (not from the bulk states). For this measurement, we used the optical setup described in the Experimental Section and Figure S15 (Supporting Information). This setup allowed spatial-frequency-filtered optical imaging, in which the position of the emission can be correlated with its direction.

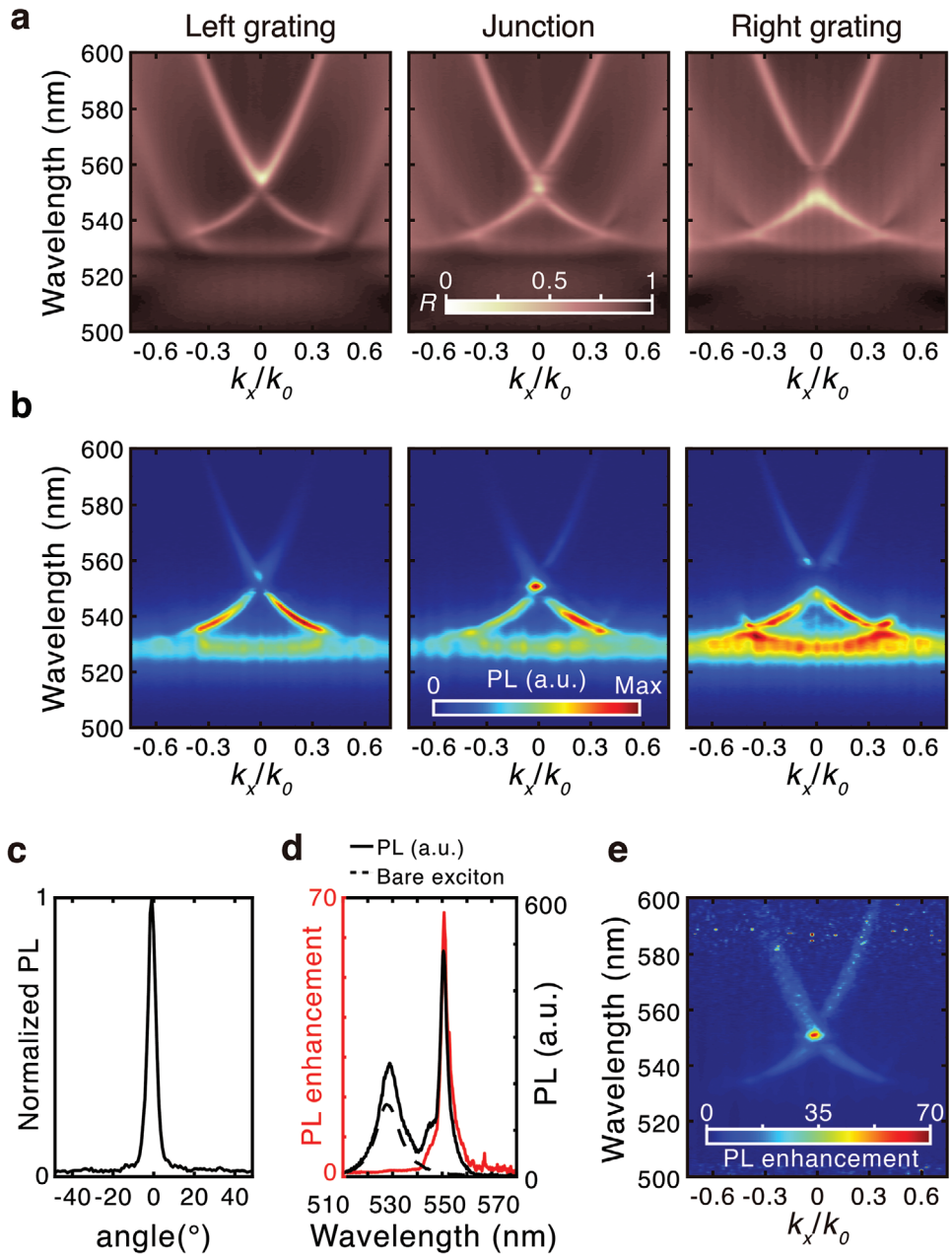

Figure 2. Angle-resolved reflectance and photoluminescence (PL) measurements. a,b) The reflectance and PL spectra of the left grating, junction, and right grating are compared. The band overlap and the JR state formation are clearly visible in both reflectance and PL spectra. The topological junction consists of 10 μm gratings on the left and right sides of the junction ($p_L = 295$ nm, $p_R = 290$ nm, $w_L = 80$ nm, $w_R = 190$ nm). Single gratings (left and right sides) have a width of 20 μm. c) Angular profile of the JR state emission. The angular divergence of the emission is 4.7°. PL enhancement factor from the junction sample d) in the normal direction ($k_x = 0$) and e) over the whole measurement range of k_x.

The optical microscopy images in the leftmost panel of **Figure 4** show the measurement conditions. The excitation laser was intentionally placed on one side of the junction (either the left or right side). As it barely touched the junction interface, both the bulk and interface states could be excited. A pinhole of 500 μm in diameter was placed in the Fourier plane (or momentum space) and gradually moved in the k_x direction ($k_y = 0$). See also Figure S16 (Supporting Information) for the spatio-spectral filtering of this measurement. In Figure 4a, we indicate the position of the pinhole as a spatial-frequency bandpass filter in the Fourier plane. The corresponding real-space PL images are shown in Figure 4b,c. At both laser excitation positions, strong PL is observed at the junction interface when the pinhole is located at the center of the Fourier plane. When the pinhole is moved away from the center, the interface emission disappears and only the PL from the bulk region remains. Combining this measurement result with the enhanced PL spectra in Figure 2, we directly confirm that the enhanced emission

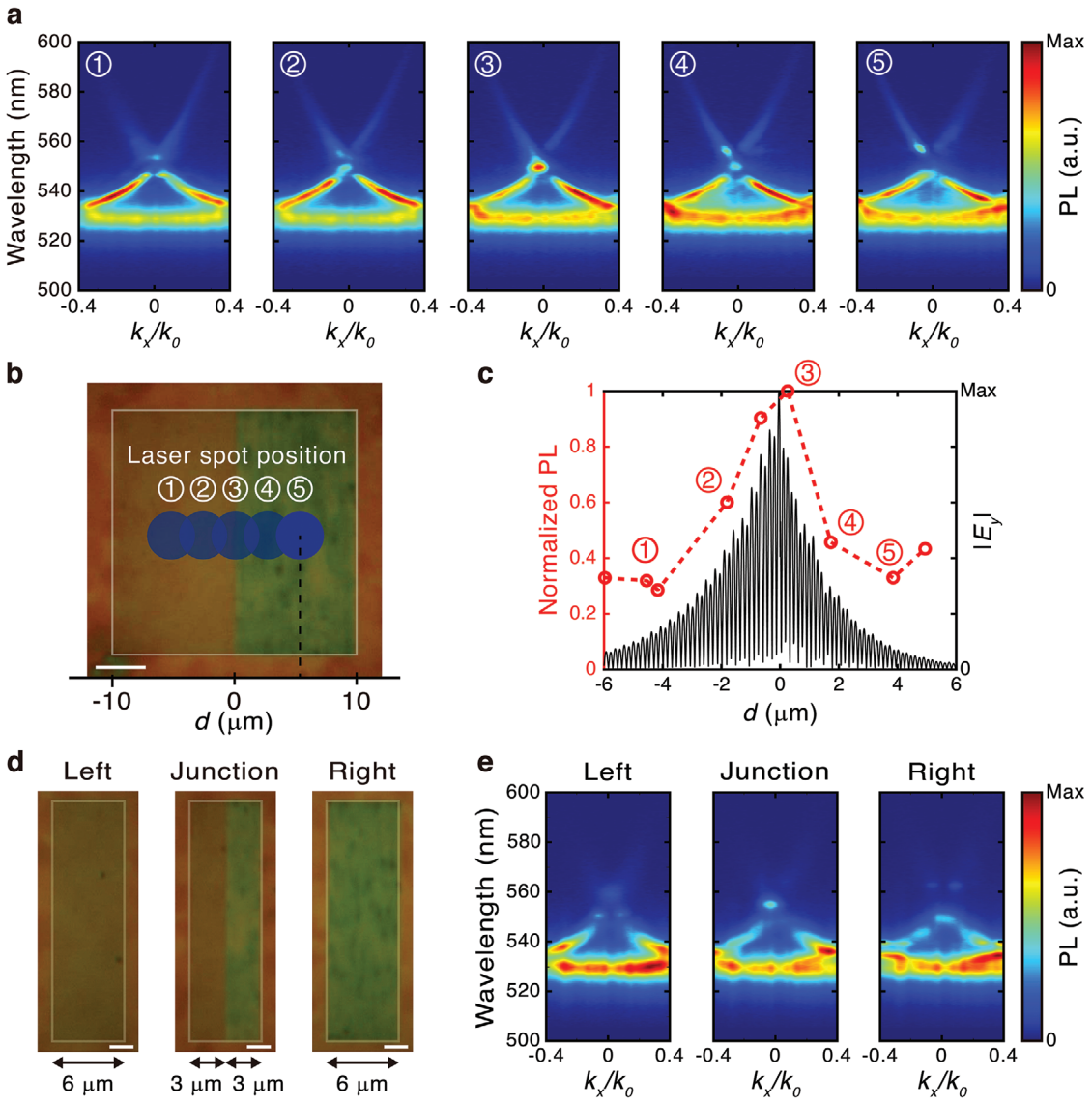

Figure 3. Topological light localization and polariton confinement. a,b) The PL spectrum is measured while the excitation laser spot is moved across the junction. The grating parameters are the same as in Figure 2. Scale bar: 4 μm. c) Plot of the JR state PL intensity as a function of the laser spot position *d*. The calculated mode profile $|E_y|$ is also shown for comparison. The JR state emission is strong only when the laser spot is located close to the junction. d,e) Optical microscopy images and PL spectra of the samples with reduced lateral sizes. The topological junction consists of 3 μm gratings on the left and right sides while the left and right gratings are 6 μm in width. The laser spot was located at the junction interface. The JR state emission remains in a tight spot while the GMR band becomes noticeably blurred. Scale bar: 2 μm.

in the normal direction indeed originates from the JR interface state.

2.5. Nonlinear Blueshift Measurements

Because the JR state enables polariton confinement near the junction interface, it may induce larger polariton nonlinearities than the delocalized GMR bands. We have experimentally verified this by comparing the PL blueshifts of the polariton JR state and GMR bands under pulsed laser excitation (**Figure 5**).

The PL blueshifts of the polariton bands were measured at two specific k_x positions (vertical dashed lines in the reflectance spectrum in Figure 5a). Figure 5b,c presents the measured data from the JR state and GMR bands. The spectral blueshift for each laser pulse fluence was determined from the PL spectrum via curve fitting. We find that, while the blueshifts remain small in the GMR band, the JR states exhibit noticeably larger blueshifts for the same laser fluence. As shown in Figure 1e, the JR state has a smaller exciton fraction than the GMR band in the shorter-wavelength region. Considering the smaller exciton fraction of the JR state, the observed nonlinear blueshift enhancement is even more remarkable. Note that larger exciton fractions are generally favored because the blueshift is caused by the excitonic component of the polaritons.[51] The additional data presented in Figure S17 (Supporting Information) further confirms this

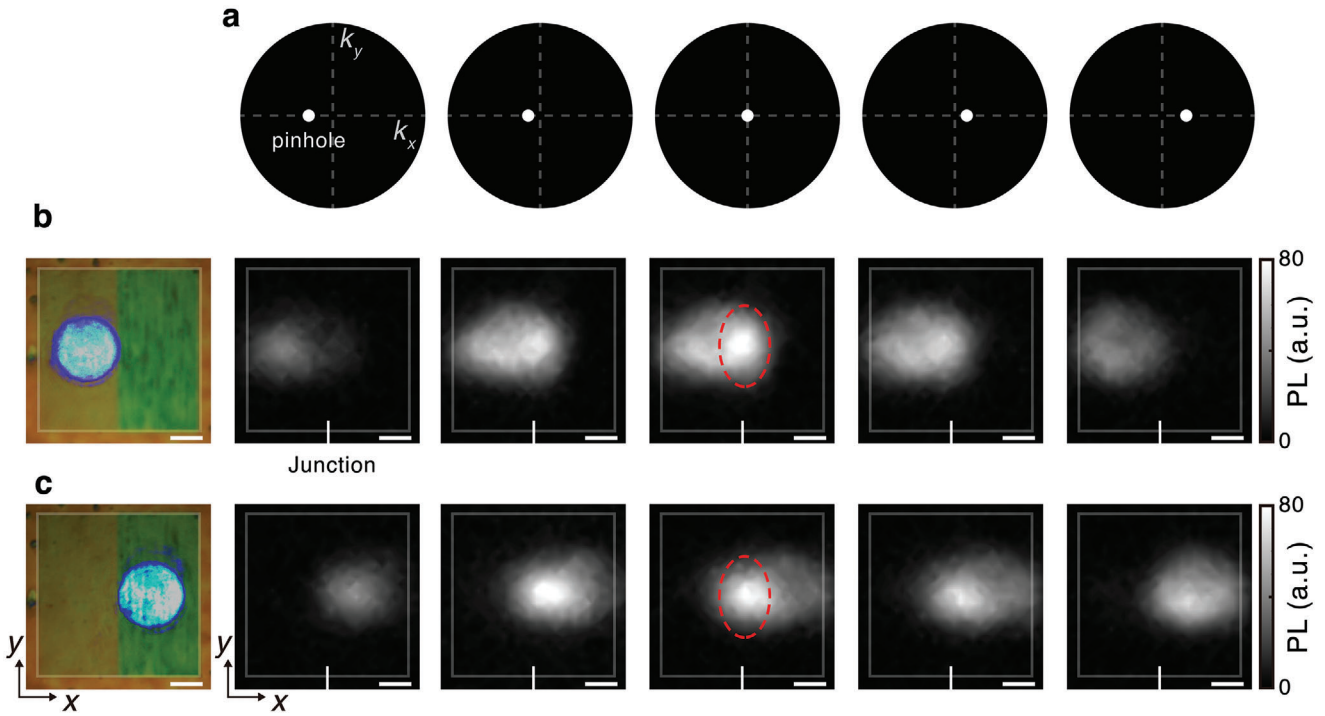

Figure 4. Real-space PL imaging with momentum-space filtering. The real-space PL images are obtained by placing a 500 μm pinhole in the Fourier plane. The excitation laser is intentionally located on one side of the junction (either the left or right side of the interface), and the real-space PL images are recorded by gradually moving the pinhole in the k_x direction: $k_x/k_0 = -0.12$, -0.04, 0, 0.04, and 0.08 in a). The topological junction consists of 10 μm gratings on the left and right sides of the junction. b,c) Only when the pinhole position is close to the JR state position, the emission at the junction interface is clearly visible. Because of the small pinhole size, we collected nearly $k_y \approx 0$ components in all cases while k_x is gradually varied. As shown in Figure S19 (Supporting Information), the polariton band is parabolic toward the higher energy in the k_y direction. However, the band is highly flat near $k_y = 0$, and thus the group velocity of the interface state is very small in the y direction. Therefore, we do not expect to observe the spreading of emission along the interface direction. Scale bar: 4 μm.

observation. Our topological light localization measurements indicate that the enhanced nonlinearity of the polariton JR state can originate from polariton confinement at the junction interface.[52–54]

Table S2 (Supporting Information) compares the polariton blueshifts in the literature with our measurements.[16,54–62] It was recently found that the blueshift value in lead halide perovskites can reach ≈20 meV.[54,62] In our case, when the laser fluence was

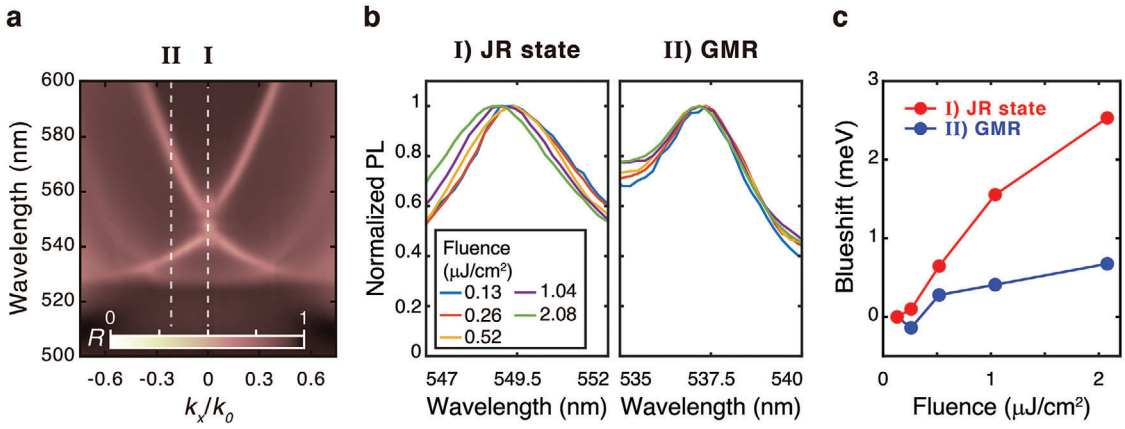

Figure 5. Nonlinear blueshift measurements. a) Reflectance spectrum of a topological junction. b,c) Measurement data at $k_x/k_0 \approx 0$ (localized JR state) and $k_x/k_0 = -0.26$ (delocalized GMR), corresponding to the vertical dashed lines in (a). The topological junction consists of 10 μm gratings on the left and right sides of the junction ($p_L = 300$ nm, $p_R = 285$ nm, $w_L = 80$ nm, and $w_R = 190$ nm). While the blueshifts remain small in the GMR band, the JR states exhibit noticeably larger blueshifts for the same range of laser fluence.

further increased, the blueshift of the polariton JR state continued to increase (Figure S18, Supporting Information). However, under such high laser fluences, the perovskite material was partly damaged. Therefore, we limited our laser fluence range to ≈2 μJ cm^{-2} in Figure 5 and Figure S17 (Supporting Information).

2.6. Further Discussion and Outlook

Polariton JR states in topological junctions have unique features in both real and momentum spaces. These systems differ significantly from other resonant exciton-polariton systems. For example, although conventional periodic optical structures, such as gratings or photonic crystals, can generate exciton-polaritons with narrow momentum-space distributions, they typically involve strong angular dispersion. They are also spatially delocalized in real space. On the other hand, strongly localized exciton-polaritons can be formed in resonant nanoparticles or nanowires. But they result in broad angular emission, which is delocalized in momentum space. The polariton JR states based on GMR gratings combine a compact spatial size with a narrow, discrete momentum-space distribution, while they are directly accessible in the normal direction. The polariton interface state and topological light localization persist as long as the bands of the two grating systems overlap. Therefore, polariton JR states can provide powerful means for tailoring exciton polariton responses in both real and momentum spaces with the additional advantage of topological robustness.

We also comment on the polariton band dispersion in the k_y direction. Figure S19 (Supporting Information) shows the reflectance spectra measured in the k_y domain at $k_x = 0$. The JR state band forms a dispersive continuum in contrast to the discrete point in the k_x domain. In principle, this is a natural consequence of the 1D localization of the JR state in linear-grating junction structures. Although the 2D localization of higher-order JR states in certain 2D-lattice junction structures may produce stronger confinement-associated enhancement effects, the delocalization of 1D JR states in the k_y direction can be potentially beneficial to efficient polariton relaxation and condensation.

Finally, we discuss possible implications of the observed polariton emission enhancement at the JR state condition. By comparing the emission enhancement spectrum (obtained under continuous-wave laser excitation) with the numerical dipole emitter simulation, we find that all the detailed features associated with the JR state resonance and GMRs as well as a certain degree of asymmetry in the experimental spectrum are well-reproduced in the numerical spectrum (Figure S20, Supporting Information). In both the experiment and simulation, the JR state exhibits a significantly larger emission enhancement than the neighboring GMR bands. However, the experimental enhancement factor is at least several times larger than the numerical value. In particular, the experimental data exhibit a noticeably larger enhancement in the JR state. Because the dipole emission calculation does not account for the dynamic distribution of polariton population along the dispersion curve,[63] it presumably indicates the increased polariton population in the JR state. In addition, the resonance feature of the JR state in the experiment is remarkably sharper in both wavelength and wavevector domains than the numerical feature. It is recently noted that a localized polariton state can be optically induced inside the photonic bandgap of 1D grating systems and the resulting polariton confinement can enhance the polariton relaxation toward the Bose–Einstein condensed state under continuous-wave laser excitation.[9,45] Because the JR state represents a similar gap-confined polariton state at $k_x = 0$, induced by topological junction structures (not by optically created potentials), we cautiously expect that polariton relaxation and the resulting coherent buildup of polariton population might be enhanced in the JR state even under low-power laser excitation. Polariton condensation in such gap-confined topological states could be the subject of further extensive follow-up studies.

3. Conclusion

We demonstrated topological exciton polaritons in a compact junction of two perovskite gratings. Detailed measurements in both momentum and real spaces revealed remarkable spatial and spectral features of the polariton interface states. The topological junction studied here provides a powerful mechanism for polariton confinement and nanophotonic light-matter enhancement, which can be tailored in both momentum and real spaces. Narrow-angled, strong polariton emissions are obtained with enhanced nonlinearities in highly simplified, compact geometries with additional advantages of topological robustness and design flexibility. A compact device size may also facilitate high-density integration on the chip. Therefore, our results suggest a promising platform for room-temperature topological exciton-polaritons and their device applications.

After the submission of the current manuscript, we found a recent article on shrunken-expanded Kagome lattices.[64] It reported a gap-confined topological state at the gamma point. However, it used metal cylinders to realize a passive topological photonic structure in the microwave regime. It did not study strongly coupled systems or exciton-polaritons.

4. Experimental Section

2D Perovskite Synthesis [$(C_6H_5C_2H_4NH_3)_2PbI_4$]: A 2:1 stoichiometric ratio of phenethylammonium iodide to lead(II) iodide was dissolved in 14 wt.% dimethylformamide (DMF) solvent to prepare the perovskite solution. The quartz substrate with the etched patterns was treated with UV ozone before spin-coating. The perovskite solution was then spin-coated onto the treated quartz at a speed of 3500 rpm for 30 s. The spin-coated film was annealed at 95 °C for 90 s.

Sample Patterning: Arrays of junction metasurface structures with different pattern parameters were fabricated on a fused quartz substrate using electron beam lithography and inductively coupled plasma reactive ion etching (ICP-RIE). The junction patterns were first created on a PMMA resist (AR-P 6200.09) using electron beam exposure and development. ICP-RIE was then conducted using SF_6, CHF_3, and Ar gases at a pressure of 5 mTorr. After quartz etching, the residual PMMA resist was removed using a resist remover (AR-600-71) in an ultrasonic bath. A 2D perovskite layer was then spin-coated onto the patterned quartz substrate and annealed for crystallization. Finally, the obtained polycrystalline film was covered with a 200 nm thick PMMA layer at a spin speed of 4000 rpm for 30 s and annealed again at 95 °C for 15 min. The perovskite materials fill the etched grating patterns on the substrates. Because the perovskite has a higher refractive index than that of the surrounding medium (PMMA and quartz), the patterned perovskite layer in the sample defines a dielectric metasurface. The etch rate of the quartz substrate

slightly depends on the width of the grating line. Therefore, a depth difference between the left and right gratings was naturally obtained. To ensure the band overlap between the left and right gratings, the period of the grating was gradually varied while the grating width and depth were fixed.

Simulation of Reflection Spectra in Single Gratings and Junction Metasurfaces: For the reflection simulations shown in Figure 1, the finite-difference time-domain method with a periodic boundary condition was used (Lumerical FDTD). In the simulations, the perovskite material was modeled in three different ways: i) a passive material with a constant refractive index of $n = 2.15$ (Figure 1c). The passive structure exhibited bare photonic modes without perovskite excitonic responses. ii) Optical constants with a single Lorentzian function were used in Figure 1d to model the effect of the perovskite excitons and show both the upper and lower polariton branches.

$$\varepsilon(\omega) = n^2 + \frac{A}{E_X^2 - E^2 - i\gamma E} \tag{7}$$

where $n = 2.15$, $A = 0.48$ eV^2, $\gamma = 0.03$ eV, and $E_X = 2.394$ eV. iii) The experimentally measured optical constants are used in Figure 1f to simulate realistic conditions. The optical constants were deduced from measurements of the transmittance and reflectance spectra.[65]

Momentum-Space Measurement of Angle-Resolved Reflectance and PL Spectra: The dispersions of the polariton bands in energy-momentum space were measured using a custom-built Fourier plane setup.[66,67] The back focal plane of the microscope objective (numerical aperture (NA) = 0.75) was imaged instead of the sample surface. For angle-resolved reflectance spectrum measurements, a collimated white-light beam was linearly polarized parallel to the grating line (i.e., transverse-electric or TE-polarized incidence). The white-light beam was then focused on the sample surface, and the intensity of the reflected beam was measured. The angle-resolved reflectance spectrum was measured in a single shot using a monochromator slit as the line aperture in the Fourier plane. The measured raw reflectance spectrum was normalized to the background reflectance of a flat silver film.

A linearly polarized continuous-wave diode laser at 450 nm was used as the excitation light source to measure the PL spectrum. The incident laser power, measured before the microscope objective, was ≈5 µW. The polariton emission from the perovskite junction metasurface was measured using a linear polarizer to collect the TE-polarized PL. All the measurements were conducted at room temperature. Both reflection and PL were measured from the PMMA side.

For the PL blueshift measurements of the polariton bands, the sample was excited with a pulse at a wavelength of 507 nm (i.e., nonresonant pumping). The pulse was generated using a Ti:sapphire laser (pulse width: ≈150 fs, repetition rate: 80 MHz) and an optical parametric oscillator, followed by second-harmonic generation. The laser spot was located at the junction interface and the diameter of the pulsed laser spot was ≈3.5 µm.

Real-Space PL Imaging: For the real-space measurements, the real-space plane was set on the entrance slit of the monochromator by changing the lens settings. For real-space PL imaging, the monochromator slit was fully opened, and the monochromator grating was set to the zero position. The PL images of the junction metasurface were recorded using a 2D charge-coupled device camera. The PL image was obtained using a 10 nm bandpass filter at 550 nm to isolate the emission around the JR state. To identify the emission from the interface state more accurately, an additional pinhole (diameter: 500 µm) was included in the Fourier plane (Figure S15, Supporting Information). The real-space PL images were recorded while the pinhole was gradually moved in the k_x direction.

Both the white light source (for reflectance measurement) and the diode laser source (for PL measurement) were focused at the junction interface. The spot size of white light was ≈11 µm in diameter. The spot sizes of the laser source were ≈4.2 µm (in Figures 2 and 3) and ≈8 µm (in Figure 4). Note that, in Figure 4, the laser spot size was intentionally enlarged to excite both bulk and interface modes.

Supporting Information

Supporting Information is available from the Wiley Online Library or from the author.

Acknowledgements

S.C.A. and Y.L. contributed equally to this work. Y.C.J. thanks Prof. Seok Ho Song for helpful discussions. Y.C.J acknowledges the support from the National Research Foundation (NRF) of Korea (NRF-2023R1A2C1004674, 2022M3H4A1A04096465) and the 2023 Research Fund (1.230013.01) of UNIST (Ulsan National Institute of Science & Technology). This research was partially supported by the Korea Institute for Advancement of Technology (KIAT) grant funded by the Korean Government (MOTIE) (P0023703, HRD Program for Industrial Innovation). J.W.Y. acknowledges the support from the NRF Leader Researcher Program (NRF-2019R1A3B2068083).

Conflict of Interest

The authors declare no conflict of interest.

Data Availability Statement

The data that support the findings of this study are available from the corresponding author upon reasonable request.

Keywords

exciton polaritons, guided-mode resonances, organic–inorganic hybrid perovskite thin films, perovskite gratings, topological junction metasurfaces

Received: November 5, 2023
Revised: March 26, 2024
Published online:

[1] A. V. Kavokin, J. J. Baumberg, G. Malpuech, F. P. Laussy, *Microcavities* (2nd ed.), Oxford Univ. Press, Oxford **2017**.
[2] D. Sanvitto, S. Kéna-Cohen, *Nat. Mater.* **2016**, *15*, 1061.
[3] D. Ballarini, M. De Giorgi, E. Cancellieri, R. Houdré, E. Giacobino, R. Cingolani, A. Bramati, G. Gigli, D. Sanvitto, *Nat. Commun.* **2013**, *4*, 1778.
[4] C. Schneider, A. Rahimi-Iman, N. Y. Kim, J. Fischer, I. G. Savenko, M. Amthor, M. Lermer, A. Wolf, L. Worschech, V. D. Kulakovskii, I. A. Shelykh, M. Kamp, S. Reitzenstein, A. Forchel, Y. Yamamoto, S. Höfling, *Nature* **2013**, *497*, 348.
[5] N. Y. Kim, Y. Yamamoto, in *Quantum Simulations with Photons and Polaritons: Merging Quantum Optics with Condensed Matter Physics*, (Eds.: D. G. Angelakis), Springer International Publishing, Cham **2017**, Ch. 5.
[6] T. Boulier, M. J. Jacquet, A. Maître, G. Lerario, F. Claude, S. Pigeon, Q. Glorieux, A. Amo, J. Bloch, A. Bramati, E. Giacobino, *Adv. Quantum Technol.* **2020**, *3*, 2000052.
[7] A. Delteil, T. Fink, A. Schade, S. Höfling, C. Schneider, A. İmamoğlu, *Nat. Mater.* **2019**, *18*, 219.
[8] G. Muñoz-Matutano, A. Wood, M. Johnsson, X. Vidal, B. Q. Baragiola, A. Reinhard, A. Lemaître, J. Bloch, A. Amo, G. Nogues, B. Besga, M. Richard, T. Volz, *Nat. Mater.* **2019**, *18*, 213.
[9] V. Ardizzone, F. Riminucci, S. Zanotti, A. Gianfrate, M. Efthymiou-Tsironi, D. G. Suàrez-Forero, F. Todisco, M. De Giorgi, D. Trypogeorgos, G. Gigli, K. Baldwin, L. Pfeiffer, D. Ballarini, H. S. Nguyen, D. Gerace, D. Sanvitto, *Nature* **2022**, *605*, 447.

[10] S. Ghosh, R. Su, J. Zhao, A. Fieramosca, J. Wu, T. Li, Q. Zhang, F. Li, Z. Chen, T. Liew, D. Sanvitto, Q. Xiong, *Photonics Insights* **2022**, *1*, R04.
[11] R. Su, A. Fieramosca, Q. Zhang, H. S. Nguyen, E. Deleporte, Z. Chen, D. Sanvitto, T. C. H. Liew, Q. Xiong, *Nat. Mater.* **2021**, *20*, 1315.
[12] J. Y. Kim, J.-W. Lee, H. S. Jung, H. Shin, N.-G. Park, *Chem. Rev.* **2020**, *120*, 7867.
[13] X.-K. Liu, W. Xu, S. Bai, Y. Jin, J. Wang, R. H. Friend, F. Gao, *Nat. Mater.* **2021**, *20*, 10.
[14] T. Ishihara, *J. Lumin.* **1994**, *269*.
[15] J.-C. Blancon, J. Even, C. C. Stoumpos, M. G. Kanatzidis, A. D. Mohite, *Nat. Nanotechnol.* **2020**, *15*, 969.
[16] A. Fieramosca, L. Polimeno, V. Ardizzone, L. De Marco, M. Pugliese, V. Maiorano, M. De Giorgi, L. Dominici, G. Gigli, D. Gerace, D. Ballarini, D. Sanvitto, *Sci. Adv.* **2019**, *5*, eaav9967.
[17] G. Lanty, A. Bréhier, R. Parashkov, J. S. Lauret, E. Deleporte, *New J. Phys.* **2008**, *10*, 065007.
[18] J. Wang, R. Su, J. Xing, D. Bao, C. Diederichs, S. Liu, T. C. H. Liew, Z. Chen, Q. Xiong, *ACS Nano* **2018**, *12*, 8382.
[19] L. Polimeno, G. Lerario, M. De Giorgi, L. De Marco, L. Dominici, F. Todisco, A. Coriolano, V. Ardizzone, M. Pugliese, C. T. Prontera, V. Maiorano, A. Moliterni, C. Giannini, V. Olieric, G. Gigli, D. Ballarini, Q. Xiong, A. Fieramosca, D. D. Solnyshkov, G. Malpuech, D. Sanvitto, *Nat. Nanotechnol.* **2021**, *16*, 1349.
[20] R. Tao, K. Peng, L. Haeberlé, Q. Li, D. Jin, G. R. Fleming, S. Kéna-Cohen, X. Zhang, W. Bao, *Nat. Mater.* **2022**, *21*, 761.
[21] K. Łempicka-Mirek, M. Król, H. Sigurdsson, A. Wincukiewicz, P. Morawiak, R. Mazur, M. Muszyński, W. Piecek, P. Kula, T. Stefaniuk, M. Kamińska, L. De Marco, P. G. Lagoudakis, D. Ballarini, D. Sanvitto, J. Szczytko, B. Piętka, *Sci. Adv.* **2022**, *8*, eabq7533.
[22] T. Fujita, Y. Sato, T. Kuitani, T. Ishihara, *Phys. Rev. B* **1998**, *57*, 12428.
[23] N. H. M. Dang, D. Gerace, E. Drouard, G. Trippé-Allard, F. Lédée, R. Mazurczyk, E. Deleporte, C. Seassal, H. S. Nguyen, *Nano Lett.* **2020**, *20*, 2113.
[24] S. Kim, B. H. Woo, S.-C. An, Y. Lim, I. C. Seo, D.-S. Kim, S. Yoo, Q. H. Park, Y. C. Jun, *Nano Lett.* **2021**, *21*, 10076.
[25] M. A. Masharin, A. K. Samusev, A. A. Bogdanov, I. V. Iorsh, H. V. Demir, S. V. Makarov, *Adv. Funct. Mater.* **2023**, *33*, 2215007.
[26] Y. Wang, J. Tian, M. Klein, G. Adamo, S. T. Ha, C. Soci, *Nano Lett.* **2023**, *23*, 4431.
[27] R. Su, S. Ghosh, J. Wang, S. Liu, C. Diederichs, T. C. H. Liew, Q. Xiong, *Nat. Phys.* **2020**, *16*, 301.
[28] S. Zhang, Q. Shang, W. Du, J. Shi, Z. Wu, Y. Mi, J. Chen, F. Liu, Y. Li, M. Liu, Q. Zhang, X. Liu, *Adv. Opt. Mater.* **2018**, *6*, 1701032.
[29] S. Klembt, T. H. Harder, O. A. Egorov, K. Winkler, R. Ge, M. A. Bandres, M. Emmerling, L. Worschech, T. C. H. Liew, M. Segev, C. Schneider, S. Höfling, *Nature* **2018**, *562*, 552.
[30] W. Liu, Z. Ji, Y. Wang, G. Modi, M. Hwang, B. Zheng, V. J. Sorger, A. Pan, R. Agarwal, *Science* **2020**, *370*, 600.
[31] M. Li, I. Sinev, F. Benimetskiy, T. Ivanova, E. Khestanova, S. Kiriushechkina, A. Vakulenko, S. Guddala, M. Skolnick, V. M. Menon, D. Krizhanovskii, A. Alù, A. Samusev, A. B. Khanikaev, *Nat. Commun.* **2021**, *12*, 4425.
[32] L. Lu, J. D. Joannopoulos, M. Soljačić, *Nat. Photonics* **2014**, *8*, 821.
[33] T. Ozawa, H. M. Price, A. Amo, N. Goldman, M. Hafezi, L. Lu, M. C. Rechtsman, D. Schuster, J. Simon, O. Zilberberg, I. Carusotto, *Rev. Mod. Phys.* **2019**, *91*, 015006.
[34] A. A. Sukhorukov, Y. S. Kivshar, *Phys. Rev. Lett.* **2003**, *91*, 113902.
[35] X. Li, E. Zhao, W. Vincent Liu, *Nat. Commun.* **2013**, *4*, 1523.
[36] M. Atala, M. Aidelsburger, J. T. Barreiro, D. Abanin, T. Kitagawa, E. Demler, I. Bloch, *Nat. Phys.* **2013**, *9*, 795.
[37] A. P. Slobozhanyuk, A. N. Poddubny, A. E. Miroshnichenko, P. A. Belov, Y. S. Kivshar, *Phys. Rev. Lett.* **2015**, *114*, 123901.
[38] P. St-Jean, V. Goblot, E. Galopin, A. Lemaître, T. Ozawa, L. Le Gratiet, I. Sagnes, J. Bloch, A. Amo, *Nat. Photonics* **2017**, *11*, 651.
[39] R. Su, S. Ghosh, T. C. H. Liew, Q. Xiong, *Sci. Adv.* **2021**, *7*, eabf8049.
[40] A. A. Gorlach, D. V. Zhirihin, A. P. Slobozhanyuk, A. B. Khanikaev, M. A. Gorlach, *Phys. Rev. B* **2019**, *99*, 205122.
[41] A. Blanco-Redondo, I. Andonegui, M. J. Collins, G. Harari, Y. Lumer, M. C. Rechtsman, B. J. Eggleton, M. Segev, *Phys. Rev. Lett.* **2016**, *116*, 163901.
[42] A. E. Hassan, F. K. Kunst, A. Moritz, G. Andler, E. J. Bergholtz, M. Bourennane, *Nat. Photon.* **2019**, *13*, 697.
[43] K. Y. Lee, K. W. Yoo, Y. Choi, G. Kim, S. Cheon, J. W. Yoon, S. H. Song, *Nanophotonics* **2021**, *10*, 1853.
[44] K. Y. Lee, S. Yoon, S. H. Song, J. W. Yoon, *Sci. Adv.* **2022**, *8*, eadd8349.
[45] F. Riminucci, A. Gianfrate, D. Nigro, V. Ardizzone, S. Dhuey, L. Francaviglia, K. Baldwin, L. N. Pfeiffer, D. Ballarini, D. Trypogeorgos, A. Schwartzberg, D. Gerace, D. Sanvitto, *Phys. Rev. Lett.* **2023**, *131*, 246901.
[46] A. Gianfrate, H. Sigurðsson, V. Ardizzone, H. C. Nguyen, F. Riminucci, M. Efthymiou-Tsironi, K. W. Baldwin, L. N. Pfeiffer, D. Trypogeorgos, M. D. Giorgi, D. Ballarini, H. S. Nguyen, D. Sanvitto, *Nat. Phys.* **2024**, *20*, 61.
[47] H. Kang, J. Ma, J. Li, X. Zhang, X. Liu, *ACS Nano* **2023**, *17*, 24449.
[48] K. Y. Lee, K. W. Yoo, F. Monticone, J. W. Yoon, *arXiv* **2023**, arXiv:2311.08766.
[49] S. S. Wang, R. Magnusson, J. S. Bagby, M. G. Moharam, *J. Opt. Soc. Am. A* **1990**, *7*, 1470.
[50] S. Fan, J. D. Joannopoulos, *Phys. Rev. B* **2002**, *65*, 235112.
[51] Y. Sun, Y. Yoon, M. Steger, G. Liu, L. N. Pfeiffer, K. West, D. W. Snoke, K. A. Nelson, *Nat. Phys.* **2017**, *13*, 870.
[52] L. Ferrier, E. Wertz, R. Johne, D. D. Solnyshkov, P. Senellart, I. Sagnes, A. Lemaître, G. Malpuech, J. Bloch, *Phys. Rev. Lett.* **2011**, *106*, 126401.
[53] T.-Y. Liu, H. Wang, M.-S. Song, L.-Y. Zhao, Z.-F. Hu, H.-Y. Wang, *Laser Photonics Rev.* **2022**, *16*, 2200176.
[54] M. A. Masharin, V. A. Shahnazaryan, F. A. Benimetskiy, D. N. Krizhanovskii, I. A. Shelykh, I. V. Iorsh, S. V. Makarov, A. K. Samusev, *Nano Lett.* **2022**, *22*, 9092.
[55] A. S. Brichkin, S. I. Novikov, A. V. Larionov, V. D. Kulakovskii, M. M. Glazov, C. Schneider, S. Höfling, M. Kamp, A. Forchel, *Phys. Rev. B* **2011**, *84*, 195301.
[56] J. Kasprzak, M. Richard, S. Kundermann, A. Baas, P. Jeambrun, J. M. J. Keeling, F. M. Marchetti, M. H. Szymańska, R. André, J. L. Staehli, V. Savona, P. B. Littlewood, B. Deveaud, L. S. Dang, *Nature* **2006**, *443*, 409.
[57] S. Christopoulos, G. Baldassarri Höger von Högersthal, A. J. D. Grundy, P. G. Lagoudakis, A. V. Kavokin, J. J. Baumberg, G. Christmann, R. Butté, E. Feltin, J.-F. Carlin, N. Grandjean, *Phys. Rev. Lett.* **2007**, *98*, 126405.
[58] V. Kravtsov, E. Khestanova, F. A. Benimetskiy, T. Ivanova, A. K. Samusev, I. S. Sinev, D. Pidgayko, A. M. Mozharov, I. S. Mukhin, M. S. Lozhkin, Y. V. Kapitonov, A. S. Brichkin, V. D. Kulakovskii, I. A. Shelykh, A. I. Tartakovskii, P. M. Walker, M. S. Skolnick, D. N. Krizhanovskii, I. V. Iorsh, *Light: Sci. Appl.* **2020**, *9*, 56.
[59] J. Zhao, R. Su, A. Fieramosca, W. Zhao, W. Du, X. Liu, C. Diederichs, D. Sanvitto, T. C. H. Liew, Q. Xiong, *Nano Lett.* **2021**, *21*, 3331.
[60] F. Barachati, A. Fieramosca, S. Hafezian, J. Gu, B. Chakraborty, D. Ballarini, L. Martinu, V. Menon, D. Sanvitto, S. Kéna-Cohen, *Nat. Nanotechnol.* **2018**, *13*, 906.
[61] R. Su, J. Wang, J. Zhao, J. Xing, W. Zhao, C. Diederichs, T. C. H. Liew, Q. Xiong, *Sci. Adv.* **2018**, *4*, eaau0244.
[62] M. A. Masharin, V. A. Shahnazaryan, I. V. Iorsh, S. V. Makarov, A. K. Samusev, I. A. Shelykh, *ACS Photonics* **2023**, *10*, 691.

[63] R. Houdré, in *The Physics of Semiconductor Microcavities* (Ed.: B. Deveaud), Wiley-VCH, Weinheim **2007**, Ch. 3.
[64] L. Tao, Y. Liu, X. Zhou, L. Du, M. Li, R. Ji, K. Song, X. Zhao, *Adv. Optical Mater.* **2023**, *11*, 2300986.
[65] R. T. Phillips, *J. Phys. D: Appl. Phys.* **1983**, *16*, 489.
[66] I. C. Seo, S. Kim, B. H. Woo, I.-S. Chung, Y. C. Jun, *Nanophotonics* **2020**, *9*, 4565.
[67] Y. Zhang, M. Zhao, J. Wang, W. Liu, B. Wang, S. Hu, G. Lu, A. Chen, J. Cui, W. Zhang, C. W. Hsu, X. Liu, L. Shi, H. Yin, J. Zi, *Sci. Bull.* **2021**, *66*, 824.